JOURNAL OF AIRCRAFT
Vol. 33, No. 3, May–June 1996

Comparison of the F/A-18A Inlet Flow Analysis with Flight Data Part 2

Steve D. Podleski* and C. Frederic Smith†
NYMA, Inc., Brook Park, Ohio 44142-1099
Wendy S. Barankiewicz‡
NASA Lewis Research Center, Cleveland, Ohio 44135-3191
and
Susan Zeleznik§
NYMA, Inc., Brook Park, Ohio 44142-1099

In this article NPARC calculations of the F/A-18A High Alpha Research Vehicle installed inlet flow are compared with flight test at a Mach number of 0.3, angles of attack of 30 and 60 deg, and nonzero sideslip angle. Predicted forebody, leading-edge extension, inlet lip, and duct surface pressures agree well with flight data. An examination of the flight-test database total pressures shows a significant degree of flow unsteadiness at the engine face. The computational results represent an asymptotic solution driven by steady boundary conditions and do not represent any particular point in time in the flight test. Therefore, comparisons of calculated inlet performance are made within a band of minimum and maximum flight-test values of inlet performance parameters. Comparisons of the predicted total pressure contours at the engine face with flight data indicate that the numerical calculations of inlet flow distortions and total pressure recovery at the engine face are at the upper and lower range, respectively, of test data, and the calculated total pressure contours are within the excursion range of the minimum total pressure, or pressure well, shown by flight data.

Nomenclature

C_p = $(P - P_\infty)/0.5\rho_\infty V_\infty^2$
FS = fuselage station in full-scale inches, 0 at 60.5 in. ahead of nose
$\dot{m}$ = mass flow rate, lbm/s
P = local static pressure, lb/ft^2
P_t = local total pressure, lb/ft^2
$P_{t_{av}}$ = average total pressure at engine face, lb/ft^2
$P_{t_{max}}$ = maximum total pressure, lb/ft^2
$P_{t_{min}}$ = minimum total pressure, lb/ft^2
P_{t_∞} = freestream total pressure, lb/ft^2
P_∞ = freestream static pressure, lb/ft^2
$T_{t_{av}}$ = average total temperature at engine face, °R
V_∞ = freestream velocity, ft/s
α = angle of attack, deg
β = angle of yaw, deg
δ = $P_{t_{av}}/14.696$ lb/in.^{2}
θ = $T_{t_{av}}/519$°R
ρ_∞ = freestream density, slug/ft^3

Introduction

PART 1 (Ref. 1) gave a brief description of the experimental program, the NPARC code and boundary conditions, the NPARC High Alpha Research Vehicle (HARV) grid model geometry and construction, and analysis procedures. This article will discuss only the differences in grid model, boundary conditions, and turbulence models from Part 1.

In this study, full Navier–Stokes calculations were completed for a combination of angles of attack of 30, 50, and 60 deg; sideslip angles of 5 and 10 deg; Mach numbers of 0.3 and 0.4; and an altitude of 25,000 ft. In this article, comparisons will be made between calculations and flight data for two cases only (see Ref. 2 for a detailed presentation of all cases): 1) angle of attack of 30 deg, sideslip angle of 10 deg, and Mach number of 0.3 and 2) angle of attack of 60 deg, sideslip angle of 5 deg, and Mach number of 0.3. The flight-test conditions are not exact duplicates of computational fluid dynamic (CFD) conditions; their average values are shown in Table 1. The discrepancies are because of the analyses being done ahead of flight tests.

The data presented consist of surface pressures along the forebody and leading-edge extension (LEX), inlet lip and duct, and the periphery of the engine face; total pressures contours at the engine face; and computer graphics-generated particle traces. A limited discussion of the calculated particle and simulated oil traces on the lower fuselage and LEX surfaces, inlet lip, and duct walls will follow. In addition, flowfield total pressures and inlet performance parameters, as measured at the engine face, will also be compared.

Experimental and Numerical Programs

To measure the effect of sideslip on inlet performance, the HARV flew at positive and negative sideslip angles since only

Table 1 Flight test conditions

Mach	α	β	Altitude
0.31	28.5	10.5	25,000
0.32	30.5	−9.0	26,000
0.31	59.0	4.0	26,500
0.32	59.0	−2.5	27,500

Presented as Paper 95-2756 at the AIAA/ASME/SAE/ASEE 31st Joint Propulsion Conference and Exhibit, San Diego, CA, July 10–12, 1995; received Sept. 26, 1995; revision received Jan. 3, 1996; accepted for publication Jan. 3, 1996. This paper is declared a work of the U.S. Government and is not subject to copyright protection in the United States.

*Senior Engineer, Propulsion Aerodynamics Section, 2001 Aerospace Parkway.
†Supervisor, Propulsion Aerodynamics Section, 2001 Aerospace Parkway. Senior Member AIAA.
‡Aerospace Engineer, Inlet and Propulsion Airframe Integration Technology Branch, 21000 Brook Park Road.
§Senior Engineering Associate, Computational Graphics Support Section, 2001 Aerospace Parkway.

the right inlet was instrumented with the rake-installed, high-frequency total pressure probes. Therefore, conditions were not exactly duplicated for the same nominal sideslip angle. Positive sideslip angle is defined as the wind coming from the pilot's right-hand side. Positive sideslip is also referred to as the windward side. Negative sideslip is referred to as the leeward side. Calculations required only one run per case since both inlets are modeled. The data were continuously corrected for changes in altitude and attitude (α, β) during a typical 6-s sampling time period.

The NPARC code was used with the Baldwin–Lomax/PD Thomas turbulence model, except for one case that was rerun with the Baldwin–Barth model to study the effect of turbulence modeling on inlet performance. Because of limited resources, all cases were not updated with the Baldwin–Barth model. The boundary conditions used for this work are similar to those used in Part 1, except that the grid was reflected across the symmetry plane, and a constant static pressure was applied to the inlet outflow or engine face. The magnitude of this pressure was determined by a desired corrected mass flow of 144 lb/s for each inlet. Therefore, the pressure applied may differ in each inlet.

The grid geometry is divided into 30 blocks, which totals approximately 2.4 million grid points.

Numerical Issues

Several convergence criteria were used. The usual monitoring of residuals was insufficient since, for turbulent flows, the residuals reach asymptote values quickly. Instead, the inlet mass flow and the inlet performance parameters were used as measures of flow convergence.

The mass flow computed at engine face was iterated over a few thousand iterations to approximately 1% of the desired value, and a mass flow ratio near 1% to a reference station near the inlet throat was usually obtained. Another convergence criteria was a change of less than 2% in flow distortion and 1% in total pressure recovery at the engine face.

In past related work done by the authors, the convergence history of external forces, lift, and drag, were monitored. It was found that these forces converged more rapidly than the inlet performance and mass flow parameters, and therefore, the external forces were not monitored for this study.

NPARC was run on the C-90 and Y-MP Cray computers; a solution of the full grid requires approximately 120 iterations per hour on the C-90 and approximately twice as long on the Y-MP. Approximately 10,000 iterations are required towards convergence, including 3000 iterations of the whole flowfield and another 7000 iterations on the ramp/splitter plate, inlet, lip, and upper diverter blocks. The grid generation process required a few weeks to reflect the previously generated symmetric grid and set up the input file.

NPARC has as an option to allow only one block to be in core memory, which helps in the rapid turnaround of jobs. The largest block of the grid model requires less than 13 Mwords of memory.

Results

External Flow

The discussion of the external flowfield will be given in two parts: 1) a comparison between test and calculations of the surface pressure on the forebody and lower LEX surfaces and 2) the calculations of particle traces generated by the forebody and lower LEX and fuselage surfaces; no flight-test-generated oilflows or tuft studies in the regions of interest were done.

Figure 1 compares the calculated and test surface pressures at five forebody and three LEX stations defined by Part 1. The circumferential angle of 0 deg on the forebody is defined as the 6 o'clock location, and increases counterclockwise, looking aft. The test conditions (Ref. 3) are not exact duplicates of calculations, but are the test conditions nearest those to calculations. At an angle of attack of 30 deg, sideslip angle of 10 deg, and Mach number of 0.3 shown in Fig. 1a, comparisons are good for fuselage stations, FS 70, FS 85, and FS 107. FS 142 shows two spikes in the pressure distribution curves. One spike, at a circumferential angle near 90 deg, is because of an antenna that is not modeled by the grid. The second spike, at a circumferential angle near 150 deg, is the footprint of the primary vortex that is not captured by calculations because of the relatively coarse gridding of the forebody. The flight test data, for circumferential angles between 0–180 deg at FS 184, show apparent problems with instrumentation. Comparisons of the surface pressure of the lower LEX surface show trends similar to the flight-test pressure profiles. The spike in the calculation curve at $z/s = 0$ is because of the definition of $z/s = 0$, which is the junction of the LEX and fuselage; the left and right LEX are separated by the fuselage diameter.

Results for the angle of attack of 60 deg, sideslip angle of 5 deg, and Mach number of 0.3 are shown in Fig. 1b. Although calculations show pressures lower than test, the comparison remains satisfactory, except for FS 107 and FS 142, where the secondary vortex peaks are stronger than that at the lower angle of attack.

FAST-generated (Ref. 4) surface oil flow and free particle traces are shown by Fig. 2a for the windward side of the aircraft, as computed by NPARC for an angle of attack of 30 deg, sideslip angle of 10 deg, and Mach number of 0.3. The restricted traces simulate oil flows or friction lines and therefore remain on the surface of the aircraft. Slightly off center of the bottom centerline of the aircraft is the attachment line that is analogous to the stagnation point on a cylinder in two-dimensional flow. A weak separation line runs along the fuselage below the LEX, and continues, although slightly weaker, on the ramp/splitter plate. Another attachment line can be seen on the nacelle, slightly behind the highlight; again, this attachment line is analogous to a stagnation point on an airfoil. A herring-bone pattern reattachment line can be seen on the underside of the LEX. The separation and reattachment lines are the footprint of a vortex that is generated by the corner of the lower surfaces of the LEX and fuselage walls. Some of this vortex is ingested by the inlet and the remainder is diverted by the ramp/splitter plate. The particle trace that is seen above the aircraft is the flow from the diverter that has been caught by a large reverse flow region above the aircraft. Figure 2b shows the restricted and free particle traces on the leeward side of the aircraft. The separation line is better defined and the vortex is stronger with a larger portion of the vortex ingested by the inlet. Particle traces show that the vortices ingested by both inlets are swallowed by the inlet boundary layer.

Surface oil flow and free particle traces on the windward side of the aircraft, as computed by NPARC for an angle of attack of 60 deg, sideslip angle of 5 deg, and Mach number of 0.3, are shown by Fig. 3a. The flow is more complex as some of the flow moves upstream in a manner similar to stagnation flow. About midway between the LEX apex and the inlet, the incoming flow is split into two, with one-half moving upstream, and the other half moving downstream; therefore, less of the vortex is ingested by the inlet. The main separation lines on the lower fuselage and reattachment lines on the lower LEX surfaces originate at midfuselage and terminate at the LEX apex for the upstream portion and at the diverter for the downstream portion. The sudden increase in curvature of the restricted particle traces on the fuselage near the ramp/splitter plate is because of the influence of the diverter wedge. The attachment line on the nacelle is further back from the highlight than at the lower angles of attack. Figure 3b shows the restricted and free particle traces on the leeward side of the aircraft. The vortices are stronger with a larger portion of the downstream vortex ingested by the inlet.

Internal Flow

Figure 4a compares the calculated and time-averaged flight-test surface pressures on the inlet lip and duct at several cir-

cumferential stations; the flight conditions are for a nominal angle of attack of 30 deg, sideslip angle of 10 deg, and Mach number of 0.3. Comparison between test and calculations is good except that peak pressures at stations 0, 90, and 225 deg are not captured; the circumferential station definition follows the convention given in Part 1. The broad pressure profile at the base of the pressure peak shown by test data at station 180 deg may imply a thick boundary layer or boundary-layer separation that is not reflected by calculations. The discontinuity in the pressure profile shown by calculation is because of the block interface between the lip and duct grids.

Comparisons of inlet lip and duct surfaces pressures for a Mach number of 0.3, an angle of attack of 60 deg, and sideslip angle of 5 deg, are shown by Fig. 4b. Again, the comparison is good, and the peak pressures are captured by calculations. Test data, again, show the broad pressure profiles at the base of the pressure peaks for stations 180 and 225 deg. Simulated oil traces, shown later, indicate flow separation on the bottom lip, but this separation is not reflected by calculated pressure profiles.

Figure 5 compares the circumferential wall pressure distribution at the engine face. Calculations assume a constant pres-

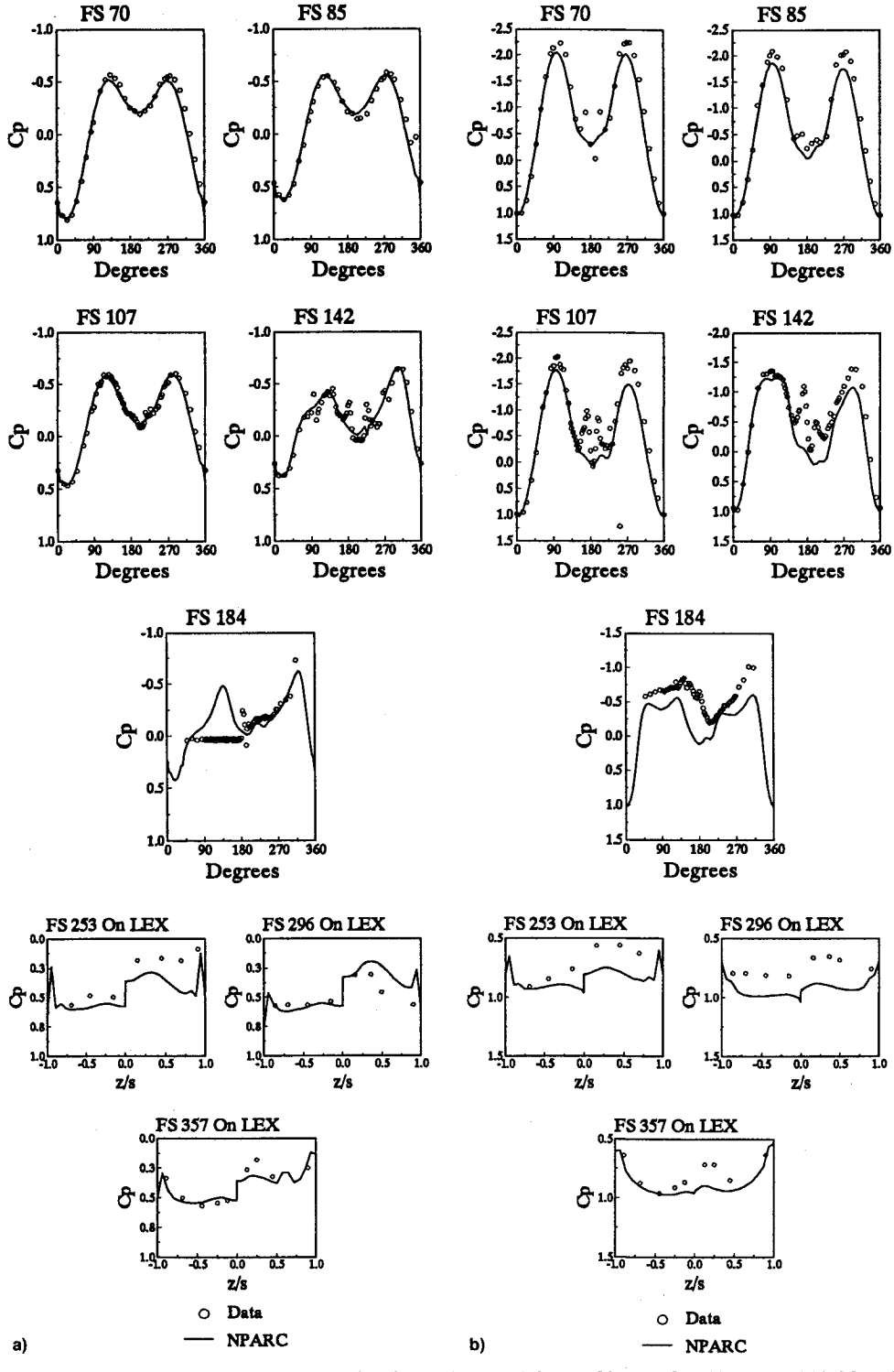

Fig. 1 Forebody/lower LEX surface static pressure distributions: a) $M_\infty = 0.3$, $\alpha = 30$ deg, $\beta = 10$ deg and b) $M_\infty = 0.3$, $\alpha = 60$ deg, $\beta = 5$ deg.

sure as a boundary condition necessary to obtain a reduced mass flow of 144 lb/s. Although the engine face was modeled as a simple constant static pressure boundary, this assumption agrees well with test data.

Next will be a discussion of the internal flowfield as described by particle traces and vortex cores generated by the FAST graphics program.

Calculated restricted and free particle traces for the windward inlet at Mach number of 0.3, an angle of attack of 30 deg, and sideslip angle of 10 deg, are shown by Fig. 6a. The restricted traces show no evidence of flow separation along the lower lip, but there is cross-stream separation as shown by a separation line that runs along the lower inboard wall of the inlet duct. The free traces that terminate in the low-pressure well at the engine face show that the origin of this flow is from the lower half of the lip. Figure 6b, a side view of the particle traces, shows a separation zone on the outboard lateral edge of the lip. A vortex lifts off the corner of the separation zone and migrates parallel to the leading edge until it is convected downstream by the unseparated flow on the lower lip where it dissipates.

For the same conditions as discussed previously, Fig. 7a shows calculated restricted and free particle traces for the leeward inlet. Again, there is no evidence of flow separation on the lower lip, but there is cross-stream separation along the lower inboard inlet duct wall. Free traces, terminating at the low pressure well at the engine face, originate from the lower lip. Fig. 7b shows a separation zone on the outboard lateral edge of the lip that is smaller than that on the windward side. The resultant vortex is weaker and quickly dissipates as it migrates parallel to the leading edge. The windward inlet lateral edge, exposed to a relative positive angle of attack induced by sideslip, would be expected to have a larger separation zone.

Figures 8a and 8b show the particle traces on the windward inlet at a Mach number of 0.3, an angle of attack of 60 deg, and sideslip angle of 5 deg. The separation zone on the lateral edge now extends to over half of the lower lip. A strong vortex lifts off the upper corner of the separation zone, migrates along the lip leading edge, and then moves downstream to terminate in the low-pressure well at the engine face.

Particle traces on the leeward inlet are shown by Figs. 9a and 9b. The separation zone, which originated from the lateral edge, now covers the whole lower lip. Two strong vortices can now be seen: one vortex originates from the upper corner of the separation zone and another vortex lifts off the lip surface from the opposite corner of the separation zone. Both vortices

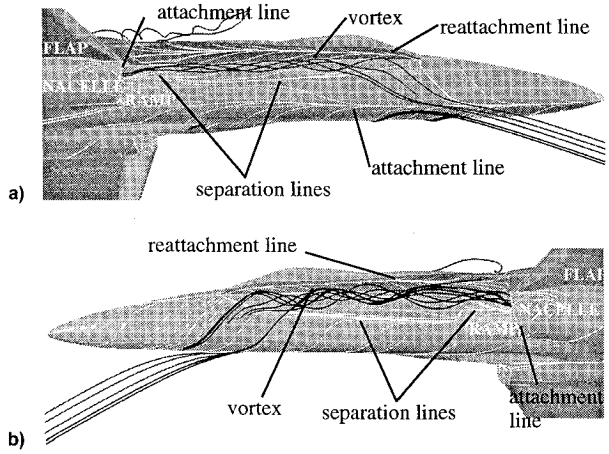

Fig. 2 Particle traces (M_∞ = 0.3, α = 30 deg, β = 10 deg): a) windward side and b) leeward side.

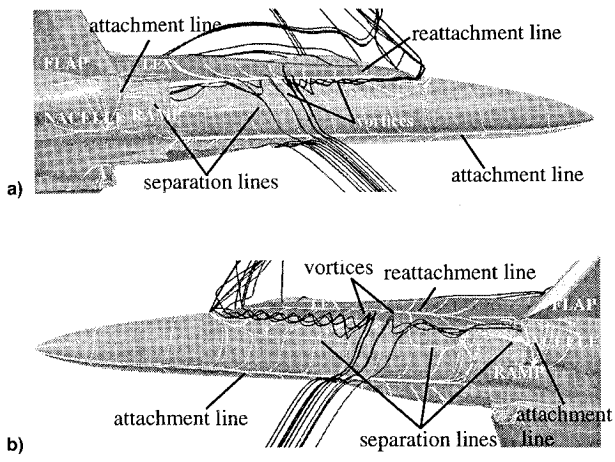

Fig. 3 Particle traces (M_∞ = 0.3, α = 60 deg, β = 5 deg): a) windward side and b) leeward side.

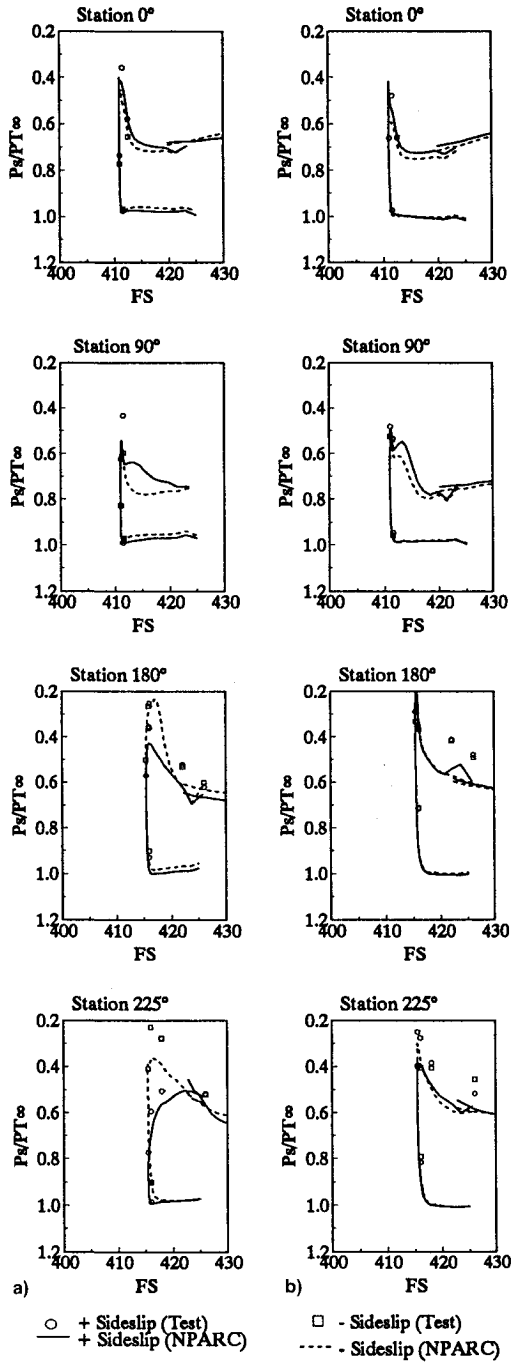

Fig. 4 Inlet lip surface pressures: a) M_∞ = 0.3, α = 30 deg, β = ±10 deg and b) M_∞ = 0.3, α = 60 deg, β = ±5 deg.

migrate down the lip until they meet at the lower inboard corner of the inlet where they are convected downstream to terminate in the low pressure well at the engine face.

Although not shown, calculations done with the Baldwin–Barth turbulence model for an angle of attack of 30 deg, a sideslip angle of 10 deg, and Mach number of 0.3, show similar simulated oil flow patterns to the Baldwin–Lomax/PD Thomas turbulence model calculations, but for a weaker liftoff vortex on the windward lip. There was no significant change in the total pressure contour topology at the engine face.

Next will be a discussion of the flowfield at the engine face. As discussed in Part 1 of this article, flight-test data show highly unsteady flow inside the inlet. The extent of crossflow separation and depth of the low-pressure region vary with time and space. NPARC was used in the asymptotic or steady-state mode. The words steady state are distinguished by their use in flight tests where they imply time averaging of test data or data obtained from low-frequency instrumentation. In CFD, steady state implies that the solution has reached a steady state, i.e., the solution does not change significantly with further iteration; steady state does not imply that the solution is the average flow if the actual flow happens to be unsteady. Therefore, the NPARC solutions represent a solution of a particular point in time as determined by the steady-state boundary conditions. The NPARC solutions were converged to a steady state as described in the Numerical Issues Section.

Discussion of inlet performance is based on the total pressure as given by the rake at the engine face. Inlet performance metrics will be given by total pressure recovery, inlet distortion intensity, known in the industry as D2, and total pressure contours. The test data total pressure contours were obtained by scanning the data and noting the frequency of occurrence of the low-pressure well at each of the rake legs. The rake legs with the two highest frequencies were used as a measure of the travel of the low-pressure well along the engine face. The test data scan also gave the min/max values of total pressure recovery and inlet distortion.

Figure 10 compares the total pressure contours of the engine face at the nominal Mach number of 0.3, an angle of attack

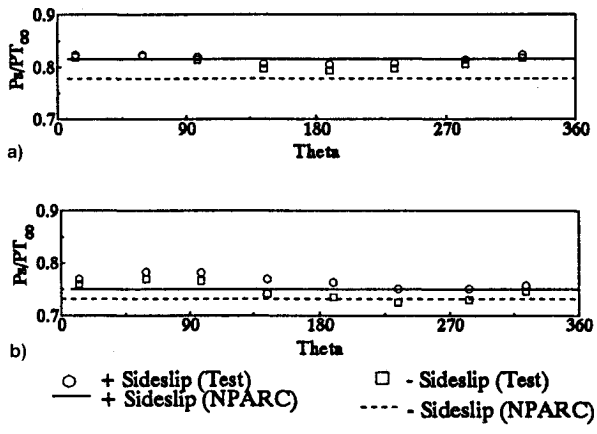

Fig. 5 Engine face circumferential surface pressures: a) $M_\infty = 0.3$, $\alpha = 30$ deg, $\beta = \pm 10$ deg and b) $M_\infty = 0.3$, $\alpha = 60$ deg, $\beta = \pm 5$ deg.

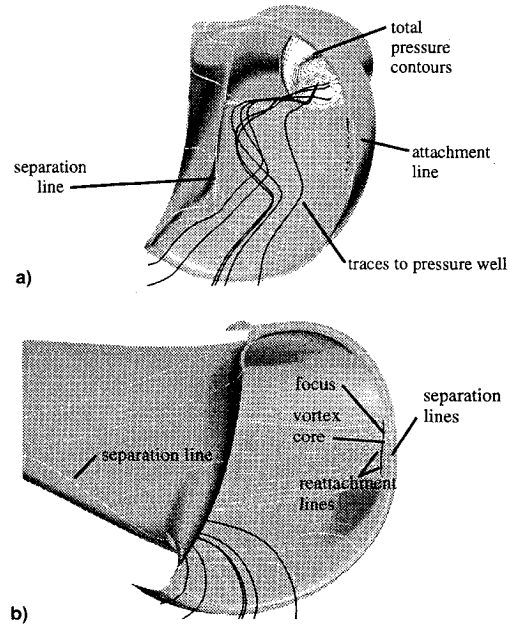

Fig. 7 Particle traces for the leeward inlet ($M_\infty = 0.3$, $\alpha = 30$ deg, $\beta = -10$ deg): a) front view and b) three-quarter view.

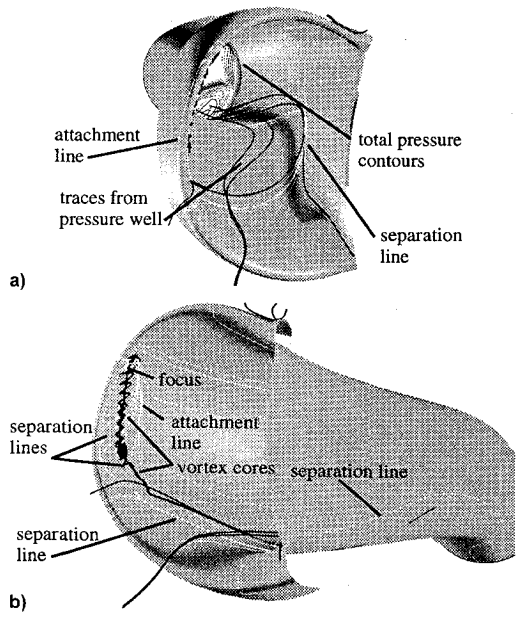

Fig. 6 Particle traces for windward inlet ($M_\infty = 0.3$, $\alpha = 30$ deg, $\beta = +10$ deg): a) front view and b) three-quarter view.

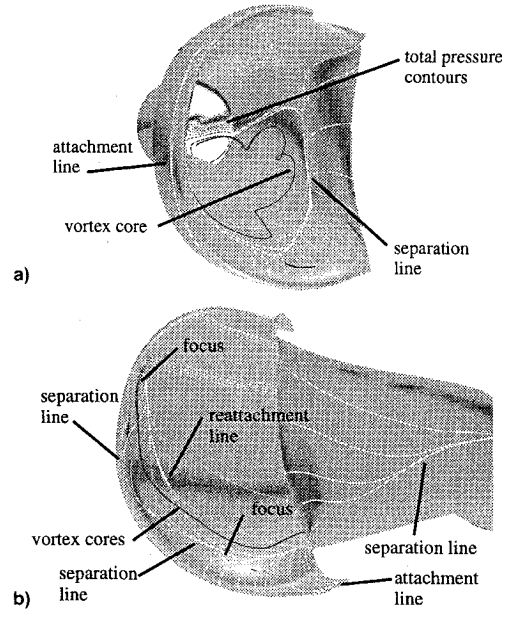

Fig. 8 Particle traces for the windward inlet ($M_\infty = 0.3$, $\alpha = 60$ deg, $\beta = +5$ deg): a) front view and b) three-quarter view.

Table 2 Inlet performance summary

	α = 30 deg, β = 10 deg		α = 60 deg, β = 5 deg	
	NPARC	Data	NPARC	Data
Windward				
$\dot{m}_{corr}$, lbm/s	143	146	144	146
Recovery, %	95	96–98	90	90–92
Distortion, %	19	9–14	29	16–33
Leeward				
$\dot{m}_{corr}$, lbm/s	145	146	144	146
Recovery, %	92	95–97	88	88–91
Distortion, %	23	10–17	35	15–34

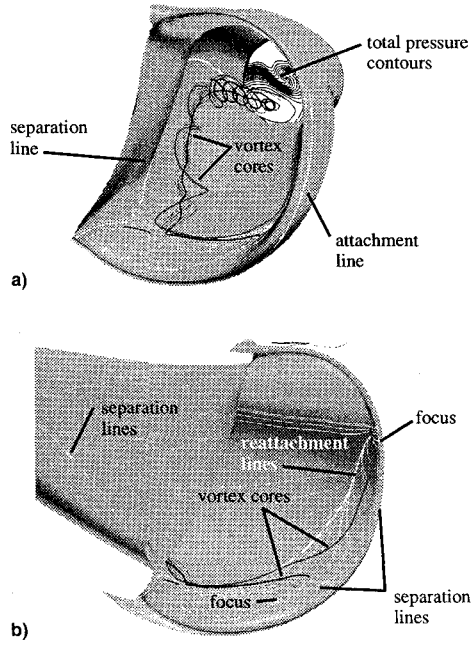

Fig. 9 Particle traces for the leeward inlet (M_∞ = 0.3, α = 60 deg, β = −5 deg): a) front view and b) three-quarter view.

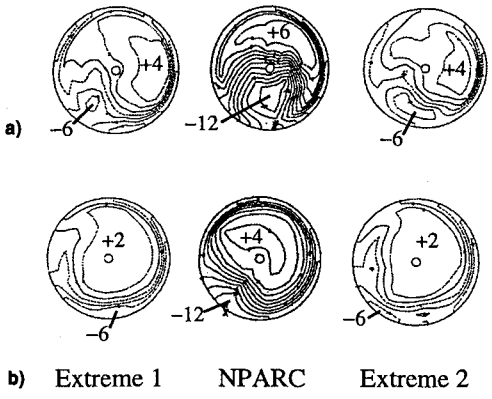

Fig. 10 Engine face normalized total pressure contours ($P_T - P_{T_{av}}$)/$P_{T_{av}}$ (M_∞ = 0.3, α = 30 deg, β = ±10 deg): a) leeward and b) windward inlets.

of 30 deg, and sideslip angle of 10 deg. The NPARC data are interpolated from the full 50 × 49 grid onto the 9 × 5 flight-test rake grid. Figure 11 compares the total pressure contours of the engine face at the nominal Mach number of 0.3, an angle of attack of 60 deg, and sideslip angle of 5 deg. Only the test contours at the most likely min/max azimuthal location of the low-pressure well are shown. Although the shape of the contours lines does not match well with test data, the calculated location of the low-pressure well falls within the range shown for the flight-test data.

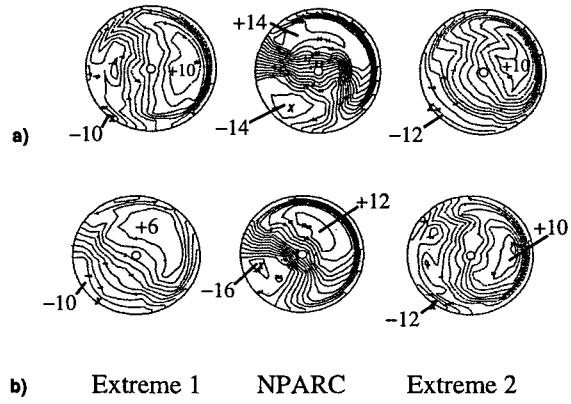

Fig. 11 Engine face normalized total pressure contours (M_∞ = 0.3, α = 60 deg, β = ±5 deg): a) leeward and b) windward inlets.

Table 2 gives a summary of the comparison of total pressure recovery and flow distortion at the engine face where a range of min/max values are given for the dynamic test data to the asymptotic CFD results. The steady-state calculations are taken from the interpolation of the CFD grid unto the flight-test rake grid. In general, the calculated performance values either lie within the min/max test band or are slightly outside the test band; calculations compare better with flight test at the higher angle of attack. In all cases, calculations and tests show that the leeward inlet has a lower performance compared to the windward inlet. This may be because of the leeward inlet being in the wake of the fuselage.

Although not shown in Table 2, the Baldwin–Barth results for an angle of attack of 30 deg, a sideslip angle of 10 deg, and a Mach number of 0.3 show a 2% point decrease in flow distortion and 1% point increase in total pressure recovery; there was no significant change in total pressure contour shape at the engine face.

Conclusions

NPARC calculations of the F/A-18A HARV were compared to flight tests, with particular emphasis to inlet performance. Calculations and tests were completed at high angles of attack and moderate sideslip for Mach numbers of 0.3 and 0.4. Comparisons of forebody and lower LEX surfaces and inlet lip and duct walls pressures are good. Although the flow is unsteady, NPARC, in a steady state or asymptotic mode, results in calculated inlet pressure recoveries that are slightly lower, but within the min/max band of test values; calculated inlet flow distortion at the fan face was slightly higher or at the high end of the min/max band of test values. Also, the engine face total pressure contours calculated by NPARC lie within the most likely zone of travel of the flight-test total pressure contours. Although the internal flow is unsteady, NPARC steady state compared relatively well with flight-test data.

The effects of sideslip provide a perturbation to the zero sideslip results. The effects of the fuselage become more sig-

nificant with a nonzero sideslip present. Local flow along the inlet lip was also influenced by the presence of sideslip.

Acknowledgments

Support of this work by the NASA Lewis Research Center under Contract NAS3-27186 is gratefully acknowledged. Interest shown by Project Manager, Thomas Biesiadny, is particularly appreciated. Thanks also to June Thompson of NASA Lewis for her contributions to setting up the data analysis system. In addition, the authors express their appreciation to Tammy Langhals and Maryann Johnston for their outstanding work in producing the text and figures for this article. Finally, we express our pleasure in working with all of the High Alpha Technology Program team members at NASA Lewis, Langley, Ames, and Dryden Research Centers, and Bill Stenkeen of the General Electric Company.

References

[1]Smith, C. F., Podleski, S. W., Brankiewicz, W. S., and Zeleznik, S. Z., "Comparison of F/A-18A Inlet Flow Analyses with Flight Data Part 1," *Journal of Aircraft*, Vol. 33, No. 3, 1996, pp. 457–462.

[2]"Evaluation of F/A-18A HARV Inlet Flow Analysis Results with Flight Data: Final Report," NASA TM, 107130, Dec. 1995.

[3]Fisher, D. F., Banks, D. W., and Richwine, D. M., "F-18 High Alpha Research Vehicle Surface Pressures: Initial In-Flight Results and Correlation with Flow Visualization and Wind-Tunnel Data," NASA TM 101724, Aug. 1990.

[4]Walatka, P. M., Clucas, J. C., McCabe, R. K., Plessel, T., and Potter, R., "FAST User Guide," NASA Ames Research Center, Moffett Field, CA, June 1993.